RSC Advances

ROYAL SOCIETY OF CHEMISTRY

www.rsc.org/advances

Table of Contents Entry:

Two derivatives of fused-arenes functionalized polyhedral oligomeric silsesquioxanes (POSS-ANT and POSS-PDI-POSS) were synthesized and their electronic properties were studied for organic – based thermoelectric devices.

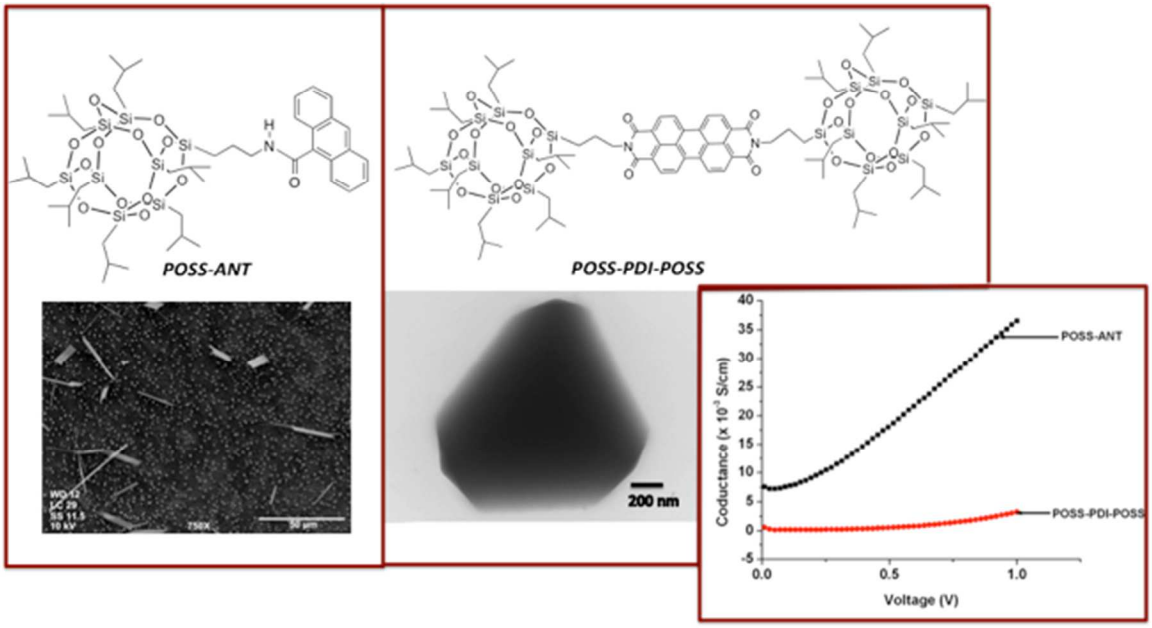

Key Words: Perylenediimide, silsesquioxanes, thermoelectric, Anthracene, Fused arenes.

*Corresponding Authors: Hemali Rathnayake –Department of Chemistry, Western Kentucky University, Bowling Green, KY 42101, Hemali.rathnayale@wku.edu; Tel. Phone – 270-745-6238.

Fused Arenes-Functionalized Polyhedral Oligomeric Silsesquioxanes as Thermoelectric Materials

*Paige Huzyak,[a] John Ferguson,[a] Jeremiah Sharpensteen,[a] Lan Xu,[a] Soundaram Jeevarathinam Ananthakrishnan,[a] and Hemali Rathnayake[a]**

Abstract. Two derivatives of fused-arenes functionalized polyhedral oligomeric silsesquioxanes (POSS-ANT and POSS-PDI-POSS) were synthesized by the reaction of aminopropylisobutyl POSS with either 9-anthracenecarboxylic acid or Perylene-3,4,9,10-tetracarboxylic dianhydride. Proton NMR and FT-IR spectroscopies confirmed their purity and structures. The UV-visible and emission spectra of POSS-ANT and POSS-PDI-POSS in solution follow similar spectral patterns as of their building blocks. These spectral signatures suggest that there is no interruption on optical properties from POSS cages. Electrical characterization conducted by casting thin films either by spin coating or drop casting on glass substrates showed subohmic semiconductor behavior with the electrical conductivity of 110.5 x 10^{-3} S cm^{-1} for POSS-ANT and 11.76 x 10^{-3} S cm^{-1} for POSS-PDI-POSS at room temperature. The temperature dependence IV curves obtained for the test devices prepared from drop casting of PDI-POSS-PDI exhibits noticeable improvement of electrical conductivity with the highest conductivity of 115.3 x 10^{-3} S cm^{-1} where as POSS-ANT shows no improvement of conductivity above the room temperature. From the temperature dependent surface morphology analysis and DSC traces, it is revealed that microstructural morphology of thin films determines almost all electrical properties of both

compounds. Thermoelectric measurement of POSS-ANT showed the maximum power factor of 2.8 μW/K^{2}m and Seebeck coefficient of 160.85 μV/K at room temperature where as POSS-PDI-POSS showed improved thermoelectric performance the above room temperature with the Seebeck coefficient of 140.30 μV/K and the power factor of 1.7 μW/K^{2}m.

Introduction

Polyhedral oligomeric silsesquioxanes (POSS) belong to the silsesquioxane family having an empirical formula of $RSiO_{1.5}$, where R may be a hydrogen atom or an organic functional group, e.g. alkyl, alkylene, acrylate, hydroxyl, or epoxide unit.[1-4] The most common POSS compounds are cage structures consisting of a silica cage core and eight organic functional groups attached to the corners of the cage. Depending on the number of organic functional groups, these molecular silica can be divided into monofunctional POSS and multifunctional POSS.[1] When all the organic groups are non-reactive, they are referred to as molecular silica. POSS nanostructures have diameters in the range 1–3 nm and, hence, may be considered as the smallest existing silica particles.[1]

Over the past decade, POSS have been used as molecular building blocks for many applications especially for electronic device applications.[5-9] These hybrid structures have been incorporated into a variety of materials to enhance their properties such as thermal stability, optical transparency, toughness, and solubility. Many of these properties are critical for applications in electronic devices, especially for organic-based optoelectronics. Significant advances have been made in incorporating POSS cages into organic light emitting materials.[7-11] Conjugated polymers functionalized with silsesquioxane cages have shown improved thermal and color stability, higher brightness, and improved quantum efficiencies compared to polymers alone.[7] Moreover, tailoring silsesquioxane cages onto light emitting conjugated polymers and

macromolecules minimizes energy trap and aggregate formation while improving the lifetime of the devices.[7] Additionally, POSS have been end-capped to π-conjugated fused-arene such as anthracene, pyrene, and perylenediimide derivatives to manipulate their self-assembly through π–π interactions to create novel multifunctional materials.[12-14] For example, Cheng et.al reported synthesis and self-assembly of perylenediimide-functionalized POSS (POSS-PDI-POSS) to study the effect of bulky and well-defined POSS nanoparticle side chains on the self-assembly behavior of perylenediimide (PDI) derivatives.[13] More recently, Jiang et.al introduced a method to make hybrid core-shell microspheres via co-assembly of multifunctional POSS end-capped anthracene with anthracene ended hyper branched poly(ether amine).[14] Although, many studies related to their electronic properties like photoluminescence, electroluminescence, and quantum efficiency have been reported,[12-14] but we are unaware of any report on evaluating their electrical properties as potential building blocks for organic thermoelectric devices. Therefore, main objective of this work is to study electrical behavior of fused-arenes functionalized POSS nanostructures under various temperature gradients as thermoelectric materials for power generation.

The current thermoelectric materials (TEs) are based on inorganic semiconductors such as bismuth telluride alloys.[15] The applicability of these materials are limited due to their high cost of production, relative scarcity, and toxicity.[15] Organic polymers and their hybrids for thermoelectric generators have emerged as possible alternatives.[16-19] Organic materials provide unique advantages in terms of mechanical flexibility, low-cost synthesis, large-scale manufacturing, and solution processability over larger areas. Moreover, organic conjugated materials possess low thermal conductivity, which gives them potentially a significant advantage over conventional thermoelectric materials. An efficient thermoelectric material must have a

very good electrical conductivity with a low thermal conductivity. However, in most materials, electrical and thermal conductivities are coupled as they both are in proportion to the concentration of the charge carriers. The key challenge in thermoelectric research is to improve electrical conductivity of thermoelectric materials without an increase of their thermal conductivity.

The performance of TEs is characterized by the figure of merit, ZT, which is defined as $ZT=S^2\sigma T/\kappa$, where S is the Seebeck coefficient, σ is the electrical conductivity and κ is the thermal conductivity.[20] $S^2\sigma$ is also known as the power factor (PF). To achieve higher ZT these three key parameters (S, σ, and κ), all of which depend on structural and morphological features, need to be manipulated.[20] Organic conducting polymers including polyaniline, polypyrrole, and poly(3,4-ethylenedioxythiophene - PEDOT) exhibit attractive thermoelectric properties,[21-24] with a power factor of about 469 $\mu Wm^{-1}K^{-2}$ reported for polymers based on PEDOT.[23] Polymer-based nanocomposites are also a promising approach to combine both the solution processibility of the conducting polymer and the good thermoelectric properties of the inorganic filler. Among them, carbon nanotube (CNT)/polymer thin films show improved thermoelectric performance with a power factor of 25 $\mu Wm^{-1} K^{-2}$ due to their heterogeneous structure.[25-29]

As the electrical conductivity of organic semiconductors depends significantly on the structural and morphological features, incorporating POSS cages may benefit the self-assembly for the formation of ordered microstructures in the solid state, resulting low thermal conductivity.[20] Nonetheless, incorporating a POSS core structure into a conjugated segment has several benefits. A siloxane core (1) serves as a robust backbone while isolating conjugated segments by connecting and aligning them in a well-defined structure, (2) minimizes materials defects, (3) able to impart high thermal and oxidative stability to the materials, and (4) enhances

solubility and film forming capability of semiconducting material. For example, previous studies in our group have shown that incorporating PDIs into bridged silsesquioxane core structures is an effective way of obtaining well-defined nanostructures as an acceptor for bulk heterojunction organic solar cells.[31]

Here, we report two compounds of PDI and anthracene end-capped POSS as potential materials for thermoelectric applications. We selected anthracene and perylenediimide moieties as our potential building blocks due to their attractive optical and electronic properties including structural flexibility, high electron mobilities, and ability to form hierarchical nanostructures through self-assembly processes.[32,33] The effect of structure-property correlation of POSS moiety on their electrical conductivities, Seebeck coefficients, and power factors were studied.

Experimental

Materials. 9-anthracenecarboxylicacid, perylene-3,4,9,10-tetracarboxy dianhydride, DCC, 200 proof anhydrous ethanol and anhydrous tetrahydrofuran were obtained from Sigma-Aldrich chemicals. Aminopropylisobutyl-POSS was purchased from Hybrid Plastics and used as received. Unless otherwise specified, all chemicals were used as received.

Characterization. Proton NMR spectra were recorded on a 500 MHz JEOL using $CDCl_3$ as a solvent. FTIR spectra were measured using a Perkin-Elmer Spectrum One FT-IR spectrometer equipped with a universal ATR sampling accessory. Thermogravimetric analysis (TGA) and differential scanning calorimetric analysis (DSC) were performed at the Thermal Analysis Laboratory at Western Kentucky University. The samples for TGA were analyzed by a TA Q5000TGA. The samples were held isothermal at room temperature for 30 min and then heated from room temperature to 650 °C at 10 °C/min in nitrogen. The purge gas was heated at 10

°C/min to 800 °C. DSC experiments were carried out on a TA Q2000 differential scanning calorimeter. The heating and cooling cycles were carried out twice for maintaining the samples' homogeneity. During the DSC experiment, the nitrogen flow rate was maintained at 50 mL/minute and standard hermatic pans were used. The samples were heated under constant flow of nitrogen to study any possible phase transitions in these materials within the temperature range of heating cycles used for electrical conductivity studies. The homogeneous samples were heated and cooled at the rate of 5°C/min. The photophysical properties in solution were performed on Fluorescence spectrometer (Perkin Elmer LS 55) and UV-visible spectrometer (Perkin Elmer, Lambda 35). Transmission electron microscopy (TEM) images were obtained on a JEOL 1400Plus TEM at 80 kV accelerating potential and images captured with an AMT XR81 digital camera. Surface features and cross sections of thin films were observed either with a JEOL 5400LV with a tungsten gun, or a JEOL 6510LV with a lanthanum hexaboride gun. Images and energy dispersive x-ray spectra were captured using IXRF system detectors and software.

Preparation of 9-anthracenecarboxyamineisobutyl-POSS (POSS-ANT): To a three-necked round bottom flask, 9-anthracenecarboxylic acid (0.500g, 2.25 mmol), aminopropyllsobutyl POSS (0.98g, 1.12 mmol), and N,N'-dicyclocarbodiimide (0.51g, 2.47 mmol) were added under an argon atmosphere. Then, anhydrous tetrahydrofuran (40.0 mL) was added and stirred continuously for ~16 hours. The resulting cloudy, yellow solution was gravity filtered, and the filtrate evaporated, leaving a sticky, dark yellow solid. This solid was dissolved in excess amount of acetonitrile (~50 mL) by sonication followed by filtration to remove dicyclohexylurea (by-products of DCC) and unreacted 9-anthracenecarboxylic acid. The crude product was further purified by repeated precipitation in chloroform: methanol 1:3 solvent mixture to remove

unreacted POSS as a solid. The filtrate was concentrated in vacuum to obtain pure product as a peach yellow solid (Yield – 85%). 1H-NMR in $CDCl_3$ {δ, ppm}: NMR, 8.33 (1H, s), 8.23-8.22 (2H,d), 7.95-7.93 (2H, d), 7.38-7.37 (4H, m), 3.23 (~1H (secondary amine), s, broad), 2.52-2.47 (2H, t), 1.81-1.71 (10H, m), 0.95-0.92 (34H, m), 0.82- 0.80 (18H, m), 0.56-0.45 (17H, two sets of m), 0.27-0.25 (2H, t); FTIR stretching (cm^{-1}): 3038 (weak, -NH stretching), 2953-2844 (C-H stretching of alkyl chains), 1567-1613 (broad, carbonyl stretching), 1458-1365 (aromatic C-C stretching), 1318-1219 (Si-C stretching), 1140-1070 (Si-O-); elemental analysis (%): experimental – C 50.80, H 7.30, N 1.60; Calculated – C 51.21, H 7.38, N 1.30.

Preparation of perylenediimide bridged-POSS (POSS-PDI-POSS): To a 100mL three-neck round-bottom flask with a stirrer bar, perylene-3,4,9,10-tetracarboxy dianhydride (0.20 g, 0.5 mmol) and aminopropyl isobutyl POSS (1.0 g, 1.1 mmol) were added. A small quantity of molecular sieve was added to the flask to absorb any excess moisture. The side necks of the flask were sealed with rubber septa and the center neck of the flask was attached to a water-cooled condenser. The flask and condenser assembly were purged with a steady flow of argon, lowered into an oil bath heated to 100 °C, and allowed to stir at 350 rpm for 10 minutes before the temperature of the oil bath was adjusted to 86 °C. After letting the temperature equalize for a minute, anhydrous ethanol (15 mL) was added by syringe. The argon flow was then stopped and the system was allowed to reflux under inert atmosphere for 24 hours. The flask was removed from the oil bath and allowed to cool to room temperature. The contents of the flask were vacuum filtered. Immediately after filtering and while still undergoing vacuum filtration, the precipitate was washed with anhydrous ethanol (30 mL). The filtrate was discarded and the precipitate was again subjected to vacuum filtration. The crude product was washed with hexane (30 mL) to remove starting material and partial products. The precipitate was then dissolved in

acetone (50 mL) and vacuum filtered. The filtrate was concentrated under vacuum to yield a bright red solid (Yield – 42%). 1H-NMR in $CDCl_3$ {δ, ppm}: NMR, 8.70-8.69 (2H, d), 8.65-8.64 (2H, d), 4.21-4.18 (2H, t), 1.85-1.81 (10H, m), 1.58 (23H, s, broad), 1.24 (2H, s), 0.95-0.92 (48H, m), 0.70-0.60 (2H, m), 0.56-0.59 (16H, m); FTIR stretching (cm^{-1}): 2953-2870 (C-H stretching of alkyl chains), 1698 (diimide carbonyl stretching), 1595 (aromatic C-C stretching), 1464 (N-C stretching from perylenediimide), 1302-1229 (Si-C stretching), 1100-1016 (Si-O-); Elemental analysis (%): experimental – C 47.95, H 6.26, N 1.60; Calculated – C 49.06, H 6.99, N 1.33.

Thickness Analysis: The film thickness of drop-casted samples was examined using a scanning electron microscope. First, the ITO coated substrates were scored with a diamond scribe on the uncoated side, cooled in liquid nitrogen, and then flexed to fracture the substrate and film beneath the score. The fractured surface was mounted face-up on a stub with the carbon tape and viewed in a JEOL 6510LV SEM at 20KV accelerating potential in low vaccum (225 mtorr) using a backscattered electron detector. The detector was set so that the brightness was related to the density and atomic number of the material. The organic film appeared as a dark layer on the substrate or as a very dark layer between bright layers for aluminum-coated films on ITO glass.

Electrical Characterization: The thin-film devices were prepared on glass/ITO substrates. The substrates were subsequently cleaned in 2- propanol and acetone in an ultrasonic bath for 15 minutes each and a layer of PEDOT:PSS (purchased from Aldrich) with a thickness of ~400-500 nm was spin coated as a hole transporting layer on top of ITO under nitrogen atmosphere. The substrates were heated at 100 °C in a vacuum oven for an hour. As a first step, the sample (either POSS-ANT or POSS-PDI-POSS) dissolved in chlorobenzene (10 mg/mL was spin coated to give a film thickness of 300-400 nm under inert atmosphere. Alternatively, the second sets of

devices were prepared by drop casting the solution on the substrate followed by slow evaporation under inert atmosphere. The substrates were transported into vacuum evaporator and a layer of aluminum (~50 nm) was thermally evaporated on top of the sample layer with a coating of 2 x 6 mm through a mask. The final devices were transferred to a glass chamber under a stream of nitrogen gas. The chamber was sealed for device characterization while maintaining the temperature of the devices at a specific temperature for five minutes. Conductivities of the samples were determined from the ohmic region of the temperature dependent IV plots obtained by a standard two probe contact method using gold-coated probes as contacts. The IV curves of the devices were measured using a Keithley 2400 source meter that connected to a PC supported with LabView. Thermovoltage at a given temperature gradient for each sample was measured directly from test devices using two-probe contacts connected to the source meter. Seebeck coefficients were obtained from the slopes of the thermovoltage (V) vs temperature gradient (ΔT) plots using the equation below.

Seebeck Coefficient, $S = {}^{\Delta V}/_{\Delta T}$ at Current Density, J = 0

Power factors were also calculated using the following equation.

Power Factor, $PF = \sigma S^2$; where σ is conductivity, V is voltage, and T is temperature in Kelvin.

Results and Discussion

Synthesis and Characterization: Scheme 1 summarizes the synthetic methodology used to make POSS-ANT and POSS-PDI-POSS. The Steglich esterification[33] of 9-anthracenecarboxylicacid with aminopropylisobutyl-POSS was performed to make POSS-ANT in considerably good yield. Since the solubility of the product and the POSS precursor are closely similar in most organic solvents, complete removal of unreacted POSS was performed by

repeated precipitation in a mixture of 1:3 chloroform to methanol followed by vacuum concentration of the filtrate.

The proton NMR spectrum of POSS-ANT and elemental analysis confirmed the assigned structure, composition, and its purity. FT-IR spectrum (**Figure S1**) further supported the formation of amide bond, based on carbonyl stretching and secondary amine N-H stretching at 1567 cm^{-1} and 3038 cm^{-1} respectively. The presence of Si-O-Si stretchings (1140 - 1070 cm^{-1}) and Si-C stretchings (1219-1318 cm^{-1}) further confirmed the successful coupling of anthracene moiety to POSS cage. The thermogravimetric data analysis (TGA) of POSS-ANT shows good thermal stability up to 215 °C with ~80% thermal decomposition at 281 °C. The complete decomposition was observed at 400 °C (See **Figure S2**).

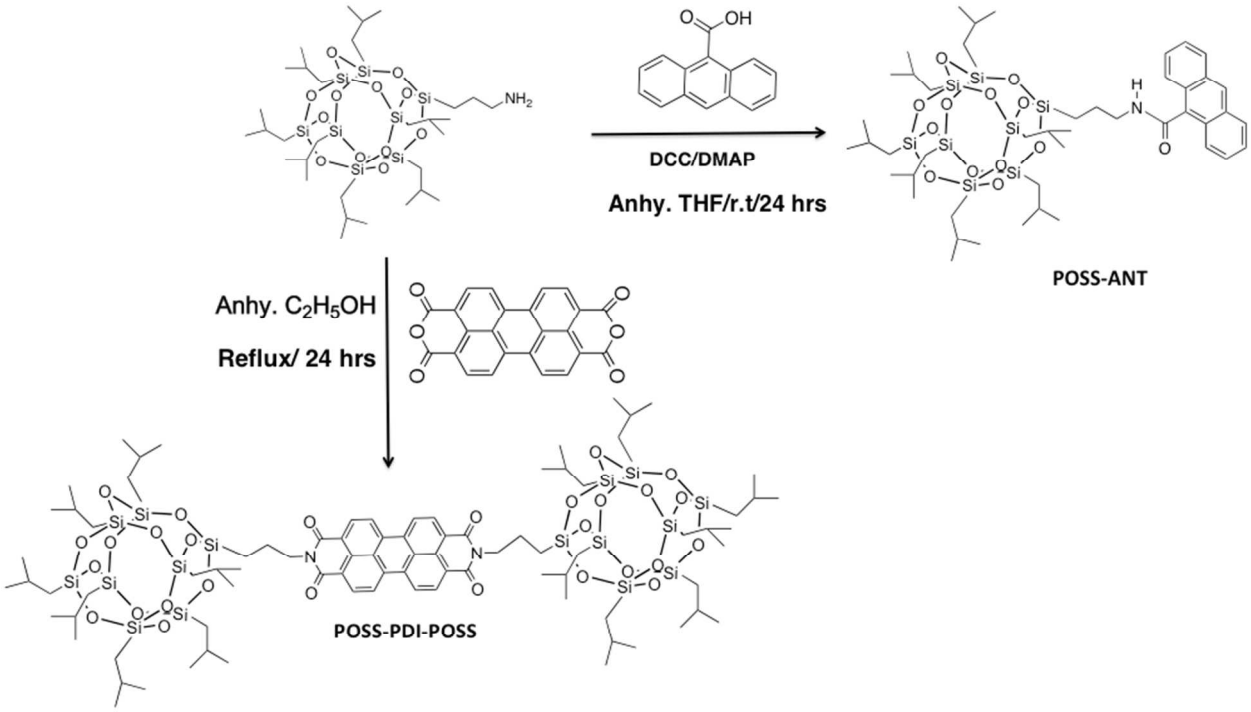

Scheme 1. Preparation of POSS-ANT and POSS-PDI- POSS

POSS-PDI-POSS was synthesized by the substitution of POSS molecules to the N-atom of the imide group in PDI as shown in Scheme 1. The preparation of POSS-PDI-POSS using typical N-

alkylation in the presence of anhydrous $Zn(OAc)_2$ in dry quinolone at high temperature conditions is well known.[13] Here, we developed a method to make POSS-PDI-POSS in considerable good yield under an environmentally friendly milder reaction condition using hot anhydrous ethanol. The product prepared in this manner was characterized by 1H-NMR, FT-IR, and elemental analysis and confirmed that the molecular structure was indeed bi-substituted. The weight loss of the organic content (57.13% at 265.14 °C), based on TGA data is in agreement with the total weight percentage of organic content obtained from elemental analysis (see **Figure S2**). The FT-IR spectra of the product confirmed the presence of characteristic bands of Si-O-Si bonds and the Si-C linkages in the POSS cage. The alkyl chains -CH and diimide carbonyl stretching vibrations were observed at 2953-2870 and 1698 cm^{-1}, respectively. The presence of aromatic C-C stretchings (1595-1660 cm^{-1}) and N-C vibrations (1464 cm^{-1}) further supports the successful incorporation of perylenediimide units to POSS core.

Photophysical Studies.

The UV/VIS-absorption and photoluminescence studies of both POSS-ANT and POSS-PDI-POSS were performed in chloroform solution. As depicted in **Figure 1a**, the solution phase absorption spectrum of POSS-ANT exhibits typical spectral characteristic features similar to molecular anthracene with three vibronic bands of the S_0-S_1 transitions at 345, 365 and 380 nm with a shoulder at 330 nm.[31] However, the fluorescence emission spectrum shows an unresolved broad peak with the peak maximum at 465 nm. The emission spectral signature of POSS-ANT agrees well with the spectral patterns of its monomer, 9-anthracenecarboxylic acid.

The absorption spectrum of POSS-PDI-POSS in chloroform has a well-resolved vibronic structure with three pronounced bands at 455, 485, 525 nm and a shoulder peak around 428 nm with an emergence of a new lower energy band centered at 580 nm. The first four absorption

peaks from left to right correspond to the vibronic bands of $S_0 - S_1$ transitions of planar PDIs.[32] The red-shifted new absorption band can be assigned to the J-aggregates, which is characteristic to the previously reported absorption spectra of aggregated PDI derivatives such as nanorods and nanowires.[34-36] To understand the nature of J-aggregates, the absorption spectra were taken for a dilution series of POSS-PDI-POSS in chloroform solution and are shown in **Figure S3**. The visibility of J-aggregates bands at lower concentrations further evidences the presence of J-aggregates in solution. The fluorescence spectrum of POSS-PDI-POSS in chloroform solution shows the expected λ_{max} at 532 nm with well-resolved vibronic bands at 574 nm and 625 nm (**Figure 1b**). These spectral patterns of the product agree well with the electronic transitions of typical planar PDIs. [13]

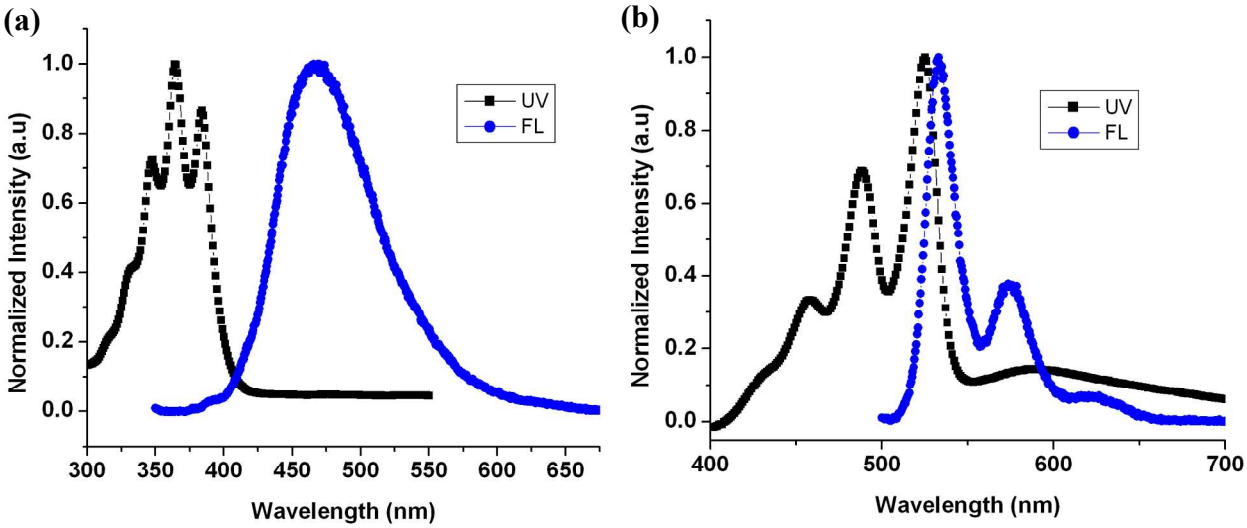

Figure 1. UV-visible and photoluminescence spectra of (a) POSS-ANT and (b) POSS-PDI-POSS in chloroform solution (Excitation, λ_{ex} = 345 nm for ANT-POSS and 488 nm for POSS-PDI-POSS).

Thin Film Morphologies.

Thin film morphologies of samples coated on either FTO coated glass substrates or carbon coated copper grids were studied under scanning electron microscope (SEM) and transmission electron microscope (TEM) and are shown in **Figure 2** & **3**. The thin film of POSS-ANT was prepared by spin coating the solution of POSS-ANT in chlorobenzene (10 mg/mL) on a pre-cleaned FTO coated glass with maintaining the spin rate of 1000 rpm for 1 minute. The SEM images of thin films of POSS-ANT exhibit random arrangements of rectangular long slates with square shape of microcrystalline objects in which most of the slates are on micrometer scale (ranging from 5 μm to 100 μm) in length and width. The square shapes crystalline objects are considerably smaller in their aspect ratios and most abundant compare to rectangular slates. The film uniformity was inconsistence and phase segregation with free spaces was abundant due to these microcrystalline objects and large aggregates throughout the film.

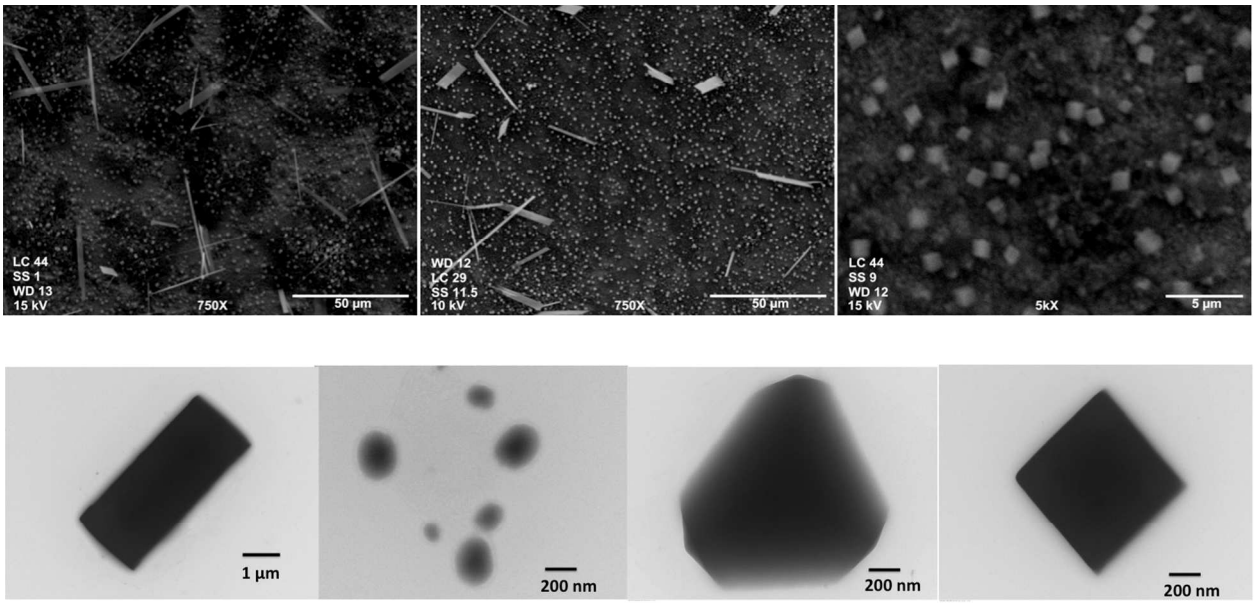

Figure 2. SEM images of thin films of POSS-ANT on glass substrate (top); TEM images of POSS-PDI-POSS coated on a carbon coated grid (bottom).

The TEM images of POSS-PDI-POSS exhibit four different shapes of microcrystalline objects, which are rectangle, spherical, triangular, and square in shapes. However, there were no large aggregates presents compare to the thin films of POSS-ANT. The aspect ratios of rectangular shapes of POSS-PDI-POSS are in the order of 5 μm of length and 2 μm in width. Surprisingly, spherical particles are on a nanometer scale with the average size ranging from 50 nm to 200 nm. However, these thin film morphologies are different from the morphologies of POSS-PDI-POSS reported by Zhuang et.al for a monolayer of Langmuir-Blodgett film of POSS-PDI-POSS.[13]

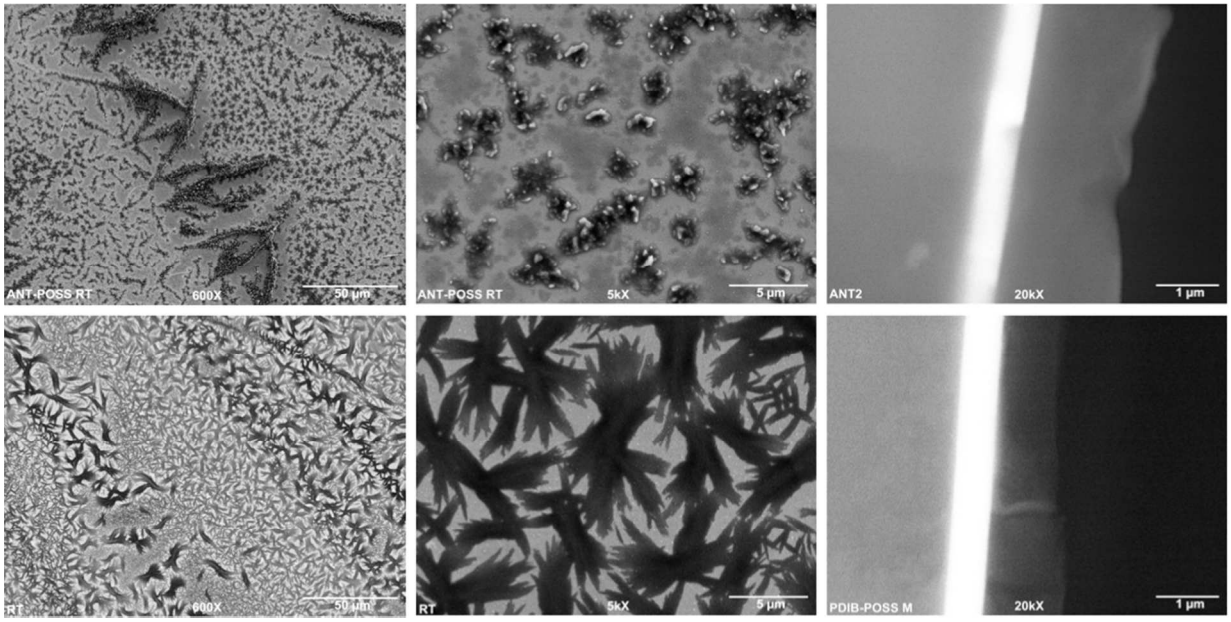

Figure 3. SEM images of drop-casted films of POSS-ANT (top) and POSS-PDI-POSS (bottom) along with the cross section of each sample film

The film morphologies of drop-casted films of both samples were also investigated by SEM analysis and compared with film morphologies of spin-coated samples. As shown in **Figure 3**, films of POSS-ANT exhibit aisles of bulky aggregates with inconsistence film morphology where as POSS-PDI-POSS films show rather smooth interconnected sheets of "spider web" morphology. It is noted that there is a clear difference in film morphology of drop-casted films of

both samples compare to the film morphology of spin-coated films. Since we speculated that the differences in thin film morphologies strongly affect to their electrical properties, we also investigated film morphologies of drop-casted films upon annealing at 50, 75, and 100 C°. The detail discussion on film morphologies of annealed samples correlating to their temperature dependent electrical properties is discussed in the follow up section of electrical properties.

The thickness of drop-casted films was analyzed by gentle fracturing of the substrate under liquid nitrogen and examined under SEM with backscattered electron detector and a detail description of the procedure is included in experimental section. The average film thicknesses of both samples were ranging from 1μm to 2 μm from the edge of the film to the middle of the film. However, we noticed that the film thickness is uneven across the films and film optimization is necessary for better electrical properties. Therefore our future work will focus on adapting a simple airbrush spray coating technique to fabricate the films with uniform thickness.

Electrical Properties.

Electrical conductivities (σ), Seebeck coefficients (S), and power factors (PF) were evaluated from test devices prepared from either spin coated or drop casted thin films of individual samples using the device configuration of Glass/ITO/PEDOT.PSS/Sample/Al. **Table 1** summarized the electrical conductivity measurements along with standard deviations of measurements for spin-coated and drop casted thin films prepared from POSS-ANT and POSS-PDI-POSS.

The current-voltage (IV) curves (**Figure 3**, **4 and S4**) for both samples show subohmic behavior with characteristic two distinct regions known as ohmic conduction and space charge limited current (SCLC) conduction. The combination of linear and non-linear behavior of IV curves was more pronounced in spin coated devices compare to the drop-cast devices. In both samples, ohmic conduction ranges from bias voltage of -0.2 to +0.2 V. In ohmic conduction,

number of free carriers remains unchanged upon the bias voltage applied where as in SCLC, the number of free carriers increases with the voltage. Therefore, material is no longer at thermal equilibrium and not following the Ohm's law ($V \propto I$). The space charge limited conduction occurs when the opposite electrodes are capable of injecting either holes or electrons in to the valence band or the conduction band of a semiconductor or an insulator.[37]Alternatively, when the rate of such carrier injection is higher than the recombination, the injected carriers will form a space charge to limit the current flow. It appears that both our samples have this conduction mechanism when the voltage exceeds ± 0.2 V. This phenomena can occur if at least one electrode contact is an ohmic contact, which is able to inject higher carrier densities over the material has in thermal equilibrium without carrier injection.[38] It may possible that at least one electrode contact of our test devices is an ohmic contact where the current voltage relation is often ohmic at low bias. However, we have not performed further studies at this point to prove that the subohmic behavior of our samples is attributed due to the ohmic type electrode contacts. Additionally, subohmic behavior is typical in disordered films as well as organic polymers and materials that are more amorphous in nature,[39] In our case, we believed that the non-linear behavior may also be attributed due to disorders from phase segregation and defects in the film as evidenced by SEM images. It is also clear from IV curves that breakdown of thin films was abundant in spin coated samples since films were too thin and easily tend to deform at higher temperatures resulting high number of trap sites in the film. This prevents overall charge recombination resulting a subohmic behavior with widely distributed bandtail.

Table 1. Electrical Conductivities of POSS-ANT and POSS-PDI-POSS

Materials	Conductivity (x 10^{-3} S/cm)							
	RT (C°)		At 50 C°		At 75 C°		At 100 C°	
	Spin and drop cast (±0.5/0.2)		Spin and drop cast (±0.02/0.6)		Spin and drop cast (±0.02/0.60)		Spin and drop cast (±0.02/0.45)	
POSS-ANT	110.5	0.13	7.16	0.23	1.33	41.66	0.60	15.30
POSS-PDI-POSS	98.0	4.45	51.76	6.60	0.039	115.3	0.001	114.2

The current-voltage (IV) curve for the spin-coated devices of POSS-ANT at room temperature shows maximum current of 4.38 mA at 1V (see **Figure 4 -** left) with the high electrical conductivity of 110.5 x 10^{-3} S/cm. As shown in **Figure 4** – right, the temperature dependent IV curves of same set of devices show significant decrease in current due to the breakdown of the film and free spaces (pinholes) from phase segregation of the film disordering at higher temperatures. As a result, the respective electrical conductivities followed the similar trend as its IV curves with significant decrease in conductivity upon the increase of temperature (see Table 1). Since we admittedly speculate the film defects and phase segregation are the main causes for poor electrical conductivity, we have performed electrical measurements on test devices prepared from drop casted films of POSS-ANT to have thicker film. As summarized in **Table 1**, electrical conductivity of POSS-ANT at room temperature was very poor not only due to the lack of film uniformity but also due to the higher thickness of the film. However, upon increasing the temperature, the conductivity gradually improved with maximum conductivity of 41.44 x 10^{-3} S/cm at 75 °C evidencing that the film is reorganized to minimize charge carrier trap sites while the film smoothens upon heating. Although we observed sudden drop in the conductivity at 100

°C, the conductivity is still high compare to the conductivity at room temperature and 50 °C for the same set of devices as well as conductivities of spin coated devices at higher temperatures.

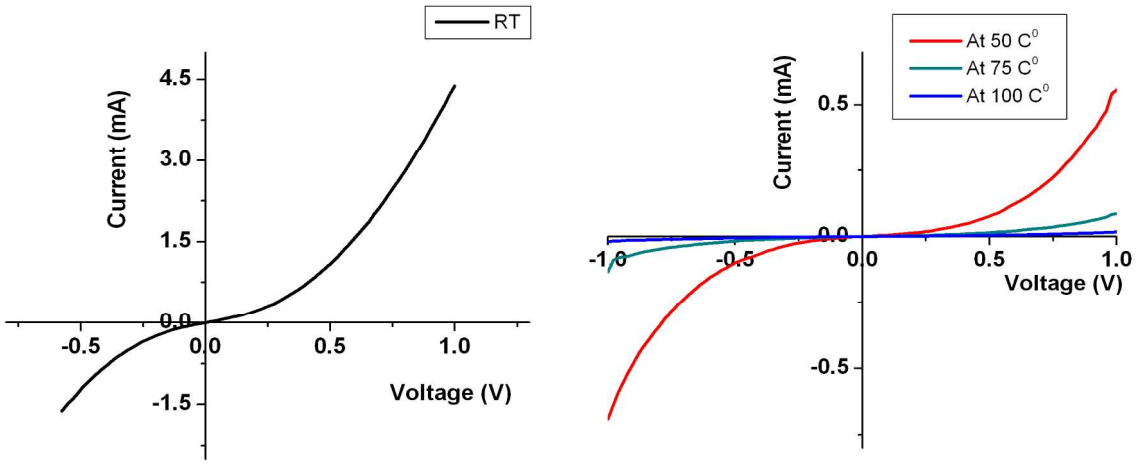

Figure 4. Current-Voltage (IV) curves for the spin-coated devices made from POSS-ANT at room temperature (left) and at three different temperatures (right)

The IV curves for both spin-coated and drop casted films of POSS-PDI-POSS at different temperatures are depicted in **Figure 5 and S4**. The IV plots of spin coated films show gradual decrease in current upon heating where as drop casted films show considerable improvement in current at higher temperatures. The spin-coated test devices gave the highest current of 3.75 mA with the conductivity of 98 x 10^{-3} S/cm at room temperature, which is slightly lower than POSS-ANT conductivity of the spin-coated devices at room temperature. However, the conductivities of spin coated thin films were drastically dropped above 50 °C evidencing the formation of defects in the spin-coated film upon heating as we observed in POSS-ANT thin films. The drop casted films show gradual increase in conductivities similar to POSS ANT drop casted films. The highest conductivities of 115.3 x 10^{-3} S/cm at 75 °C and 114.2 x 10^{-3} S/cm at 100 °C were resulted with rather linear IV curves upon heating.

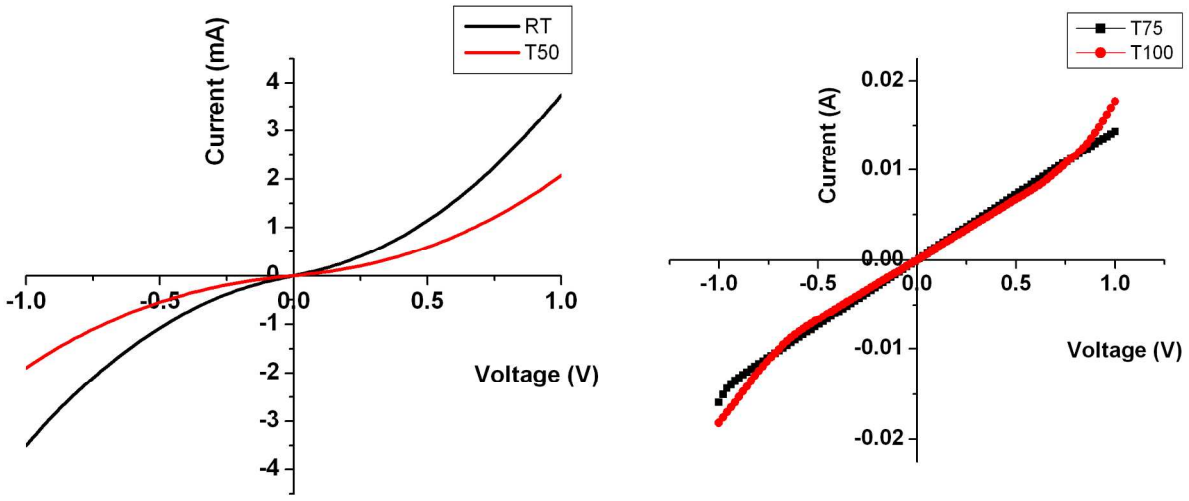

Figure 5. IV curves of POSS-PDI-POSS at different temperatures for the devices made from spin coated (right) and drop casted (left).

These findings suggest that microstructural morphology and film thickness play a major role on electrical performance. As drop-casted films of both samples showed significant difference in electrical conductivities, more in-depth structural characterizations were performed from surface morphology studies, IR, and differential scanning colorimetric analysis (DSC). Microstructural morphologies of drop-casted films at each temperature were evaluated using SEM and are shown in **Figure 6** and **7**.

The drop-casted film of POSS-ANT at room temperature shows an irregular surface with randomly distributed clusters due to the uneven drying of solution droplets. The clusters were better distributed upon heating to 50 °C, showing larger aggregates were rearranged to smaller size aggregates, which provides indirect evidence of the availability of good electrical pathways across the film. As a result, the electrical conductivity was gradually increased with temperature, yielding the highest electrical conductivity at 75 °C. However, the reduction of electrical

conductivity at 100 °C could be attributed to phase segregation of the film as indicated by the thicker clusters in the SEM image of 100 °C.

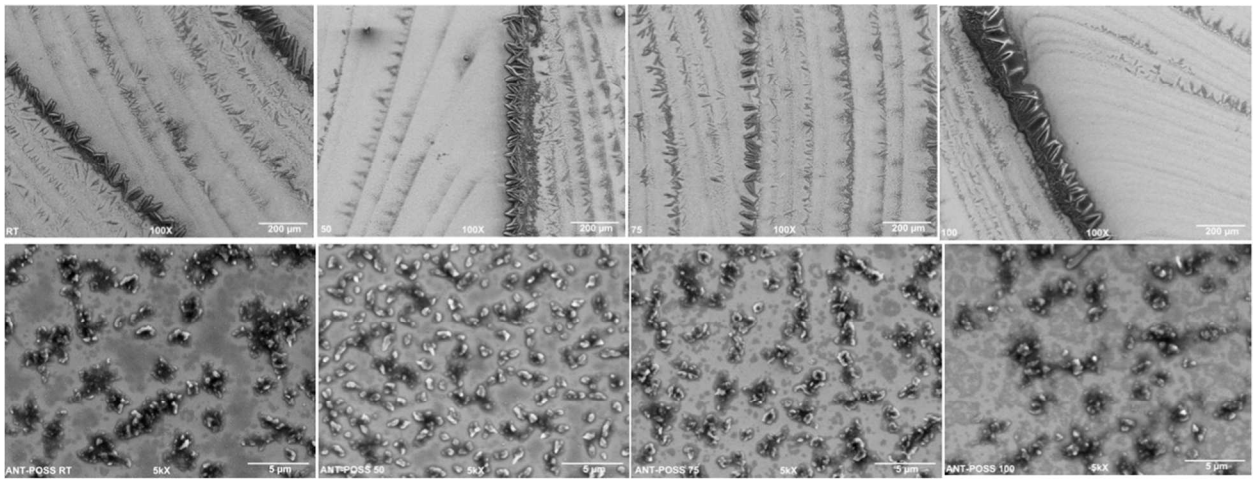

Figure 6. SEM images of drop casted films of POSS-ANT at room temperature and after annealed to 50, 75, and 100 °C (from left to right); scale bar – 200 µm (top images) and 5 µm (bottom images)

The phase behavior of POSS-ANT observed from DSC traces was in good agreement with the intrinsic microstructural changes observed in SEM micropgraphs. As shown in **Figure S5**, the DSC scans of reversible heating and cooling cycles show a distinct reversible phase transitions at peak maxima of 34.69 C° and 24.60 °C with the enthalpy changes (ΔH) of 3.71 J/g and 3.62 J/g, indicating the occurrence of intrinsic phase changes in the film upon heating and cooling. The heating curve also shows two additional broader transitions at 77.18 °C and 143.40 °C with slight change in enthalpy, while cooling curve shows an additional extended broad phase transition 46.82 °C with minimal enthalpy change of 0.18 J/g. From these multiple reversible phase transitions of DSC thermograms, it could be concluded that electrical performance of POSS-ANT depends on its microstructural morphology.

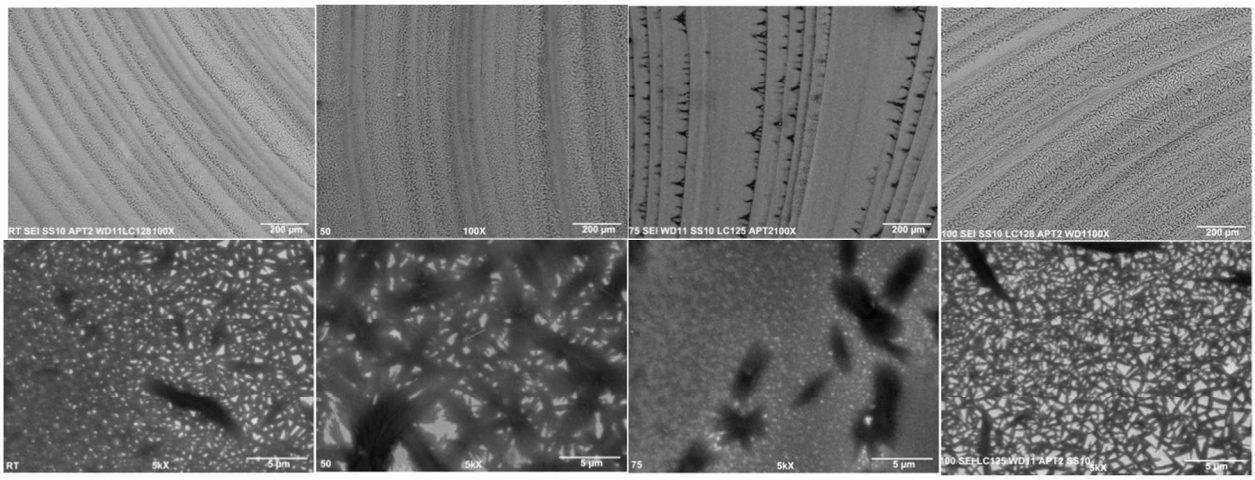

Figure 7. SEM images of drop casted films of POSS-PDI-POSS at room temperature and after annealed to 50, 75, and 100 °C (from left to right); scale bar – 200 μm (top images) and 5 μm (bottom images)

The microstructures of POSS-PDI-POSS drop casted films were very different from those of segregated clusters of POSS-ANT and were distributed rather evenly across the film with more interconnected sheets and spaghetti like structures. The clear indication of microstructural changes in thin films was observed upon annealing to each temperature gradient. As shown in **Figure 7**, the wrinkle patterns of the films tend to more dispersive gradually and a decrease in porosity was observed with temperature. The SEM images taken after annealed to 75 °C show much smooth surface with minimal void spaces in the film compared to the SEM images taken at room temperature, and 50 °C. However, micro-voids start to re-appear after annealed to100 °C, evidencing that the film microstructure was deformed. According to these SEM micrographs, it is obvious that formation of micro-voids disconnects the favorable electrical pathways across the film and as a result we observed a huge difference in the temperature dependent electrical conductivities of POSS-PDI-POSS. The DSC traces of POSS-PDI-POSS were in favor of such microstructural changes observed in SEM analysis. As shown in **Figure S6**, POSS-PDI-POSS exhibits a broad reversible phase transitions of heating and cooling cycles with the corresponding

peak maximum for heating at 87.26 °C and corresponding reversible cooling phase transition at 72.82 °C with the enthalpy change of 1.10 J/g. The phase transition observed correlates with the microstructural changes observed at 75 °C and 100 °C as well as the sharp jump in conductivity at 75 °C.

In order to confirm that there is no structural degradation or bond stretching rearrangements of both compounds after annealed to the selected temperature gradients, we performed IR analysis for both samples after heated to each temperature. It is worth to note here that these IR analyses were not performed while the substrate was heating. Samples were heated and cooled down to the room temperature under inert atmosphere and IR traces were obtained. As shown in **Figure S11**, both samples show no indication of structural changes or bond stretching rearrangements of bond breaking within the temperature range of 50 to 100 °C.

Overall, both samples show promising electrical conductivities at room temperature and POSS-PDI-POSS shows better electrical conductivity at higher temperatures compare to that of for POSS-ANT. However, the magnitudes of electrical conductivities are still low as thermoelectric materials for potential applications. In order to improve the electrical conductivities without sacrificing their Seebeck coefficients, we will conduct electrical measurements by doping the samples with dopants like iodine and p-toluenesulfonic acid and by blending with organic conjugated block copolymers. As previously reported, doped conjugated polymers including MEH-PPV and block copolymers of oligo-phenylvinylenes showed much improved electrical conductivities with promise as organic thermoelectric materials.[40]

Table 2. Seebeck coefficients and Power factors of POSS-ANT and POSS-PDI-POSS

Materials	Seebeck Coefficient (μV/K)		Power Factor (x 10^{-3} W/K^2 m)	
	Spin-coated film (± 2.10)	Drop-casted film (±1.80)	Spin-coated film at RT (± 0.50)	Drop-casted film at 75 °C (± 0.35)
POSS-ANT	160.85	74.71	2.8	1.0
POSS-PDI-POSS	123.83	148.30	1.5	1.7

The Seebeck coefficients of both samples were obtained from slopes of voltage against temperature gradient curves (See **S7 – S8**) for both spin coated films and drop casted films and are summarized in **Table 2**. Seebeck coefficients of POSS-ANT were found to be 160.85 μV/K for spin-coated film and 74.71 μV/K for drop-casted film, where as POSS-PDI-POSS shows Seebeck coefficients of 123.83 μV/K and 148.3μV/K for spin-coated and drop-casted films respectively. Both samples show comparable Seebeck coefficients for spin coated devices where as POSS-PDI-POSS shows two fold higher Seebeck coefficient compare to POSS-ANT for drop casted films. The lower Seebeck coefficient of drop casted POSS-ANT is low as its conductivities were poor at higher temperatures compare to the conductivities of POSS-PDI-POSS drop-casted films. Overall, both samples' Seebeck coefficients follow a linear relationship with their conductivities.

The power factor (PF = $S^2\sigma$), which measures the thermoelectric performance of a materials was also calculated for both samples at room temperature and at 75°C and summarized in **Table 2.** Generally, a good balance between conductivity and Seebeck coefficient is required to obtain a maximum power factor. The power factors obtained for POSS-ANT are 2.8 x 10^3 μW/K^2 m at room temperature and 1.0 x 10^3 μW/K^2 m at 75 C°. The power factor of POSS-ANT at room

temperature is higher than the power factors of polycarbazole derivatives reported in literature.[24] However, at higher temperatures, the power factor of POSS-ANT decreased due to the significantly low conductivities specially in spin-coated thin films. As expected, although the power factor of POSS-PDI-POSS is slightly lower than POSS-ANT at room temperature, the power factor at 75 C° is much improved in drop-casted films.

These electrical conductivities and thermoelectric measurements suggest that the fused-arene functionalized POSS are promising as thermoelectric materials and incorporating POSS cages play an important role on device performance and materials stability. Both POSS-ANT and POSS-PDI-POSS performed well as a thermoelectric material at room temperature and POSS-PDI-POSS is also promising higher temperatures of 75 C° and 100 C° compare to POSS-ANT. In overall, both materials make promising for the thermoelectric devices, which operates at lower temperatures.

Conclusion

Here, we demonstrated the potential applicability of fused arene-functionalized POSS nanostructures for organic-based thermoelectric devices. Thin film morphologies, optical, and preliminary characterization of thermoelectric properties of the derivatives of anthracene (POSS-ANT) and PDI (POSS-PDI-POSS) functionalized POSS were investigated. POSS-ANT was found to be a promising candidate having a maximum power factor of 2.8 x 10^3 $\mu W/K^2$ m and the electrical conductivity of 110.5 x 10^{-3} S/cm at room temperature. POSS-PDI-POSS showed better electrical performance at 75 C° and 100 C° and having a promise as thermoelectric materials for the temperature range of 75 C° to 100 C°. Future studies will focus on optimizing the film morphology and film thickness using a simple spray coating technique and improving the thermoelectric performance through doping the materials. Nonetheless, as this is the first

example of investigating thermoelectric properties of fused arenes-functionalized POSS, we believe these findings will contribute to the development and utilization of POSS functionalized nanomaterials for organic – based TEGs, which operates at lower temperatures.

Acknowledgements

The authors gratefully acknowledge the financial support from Office of Research Foundation at WKU (RCAP- 13-8042), Kentucky Science & Engineering Foundation (KSEF-3030-RDE-017), NSF-EPSCoR-R-REG (Y6_Bridge), NSF-CHE-MRI under the Award ID of 1338072, and NSF-MRI under the Award ID of 1429563. We are pleased to acknowledge Dr. John Andersland for SEM support, Pauline Norris at Advanced Materials Institute and Jacob Strain for elemental analysis, Quentin Lineberry for TGA analysis and thermal analysis lab for DSC analysis.

Notes and references

[a]*Department of Chemistry, Western Kentucky University, Bowling Green, KY 42101;*

**Corresponding Authors: Hemali Rathnayake –Department of Chemistry, Western Kentucky University, Bowling Green, KY 42101, Hemali.rathnayale@wku.edu; Tel. Phone – 270-745-6238.*

† Electronic Supplementary Information (ESI) available: Experimental procedures are available in supporting information section. See DOI: 10.1039/b000000x/.

1. S.-W. Kuo, F.-C. Chang, *Prog. Polym. Sci.* 2011, **36**, 1649–1696.
2. D. B. Cordes, P. D. Lickiss, F. Rataboul, *Chem. Rev.* 2010, **110**, 2081–2173.
3. K. J. Shea, D. A. Loy, *Chem. Mater.* 2001, **13**, 3306–3319.
4. L P. D. Lickiss, F. Rataboul, In *Advances in Organometallic Chemistry*, Anthony F. Hill and Mark J. Fink, Ed.; Academic Press, 2008, **57**, 1–116.

5. C.-M. Leu, Y.-T. Chang, K.-H. Wei, *Chem. Mater.* 2003, **15**, 3721–3727.

6. E. Tegou, V. Bellas, E. Gogolides, P. Argitis, D. Eon, G. Cartry, C. Cardinaud, *Chem. Mater.* 2004, **16**, 2567–2577.

7. N. Vourdas, V. Bellas, E. Tegou, O. Brani, V. Constantoudis, P. Argitis, A. Tserepi, E. Gogolides, D. Eon, G. Cartry, C. Cardinaud, *Plasma Process and Polymers,* Wiley-VCH: Weinheim, Germany, 2005, 281.

8. A. Sellinger, R. M. Laine, US6517958 B1, 2003.

9. S. Xiao, M. Nguyen, X. Gong, Y. Cao, H. Wu, D. Moses, A. J. Heeger, *Adv. Funct. Mater.* 2003, **13**, 25–29.

10. A. C. Arias, J. D. MacKenzie, I. McCulloch, J. Rivnay, A. Salleo, *Chem. Rev.* 2010, **110**, 3–24.

11. R. Tipnis, J. Bernkopf, S. Jia, J. Krieg, S. Li, M. Storch, D. Laird, *Sol. Energ. Mat. Sol. C.* 2009, 93, 442–446.

12. X. Ren, B. Sun, , C.-C. Tsai, Y. Tu, S. Leng, K. Li, Z. Kang, R. M. V. Horn, X. Li, M. Zhu, C. Wesdemiotis, W.-B. Zhang, S. Z. D. Cheng, *J. Phys. Chem. B* 2010, **114**, 4802–4810.

13. X-D. Zhuang, Y. Chen, B. Zhang, Y. Li, B. Yu, W. Qiao, *New J. Chem.* 2010, **34**, 1120–1124.

14. Z. Su, B. Yu, X. Jiang, J. Yin, *Macromolecules* 2013, **46**, 3519–3528.

15. H. J. Goldsmid, *Recent Trends in Thermoelectric Materials, Semiconductors and Semimetals.* Academic, 2000, **69**, Chapter 1.

16. N. Dubey, M. Leclerc, *J. Polym. Sci. B Polym. Phys.* 2011, **49**, 467–475.

17. H. Yan, T. Ohta, N. J. Toshima, *Macromol. Mater. Eng.*, 2001, **286**, 139-142.

18. H. Yan, N. Sada, N. J. Toshima, *J. Therm. Anal. Calor.*, 2002, **69**, 881-887.

19. N. Toshima, *Macromol. Symp.*, 2002, **186**, 81-86.

20. M. S. Dresselhaus, G. Chen, M. Y. Tang, R. G. Yang, H. Lee, D. Z. Wang, Z. F. Ren, J.-P. Fleurial, P. Gogna, *Adv. Mater.* 2007, **19**, 1043–1053.

21. L. Jun, Z. Lian-meng, H. Li, T. Xin-Feng, *J. Wuhan Univ. Technol.-Mat. Sci. Edit.* 2003, **18**, 53–55.

22. N. T. Kemp, A. B. Kaiser, C.-J. Liu, B. Chapman, O. Mercier, A. M. Carr, H. J. Trodahl, R. G. Buckley, A. C. Partridge, J. Y. Lee, C. Y. Kim, A. Bartl, L. Dunsch, W. T. Smith, J. S. Shapiro, *J. Polym. Sci. B Polym. Phys.* 1999, **37**, 953–960.

23. G-H. Kim, L. Shao, K. Zhang, K. P. Pipe, *Nature Materials.* 2013, **12**, 719-723.

24. X. Crispin, S. Marciniak, W. Osikowicz, G. Zotti, A. W. D. Van der Gon, F. Louwet, M. Fahlman, L. Groenendaal, F. De Schryver, W. R. Salaneck, *J. Polym. Sci. B Polym. Phys.* 2003, **41**, 2561–2583.

25. Q. Yao, L. Chen, W. Zhang, S. Liufu, X. Chen, *ACS Nano* 2010, **4**, 2445–2451.

26. C. Yu, Y. S. Kim, D. Kim, J. C. Grunlan, *Nano Lett.* 2008, **8,** 4428–4432.

27. D. Kim, Y. Kim, K. Choi, J. C. Grunlan, C. Yu, *ACS Nano* 2010, **4**, 513–523.

28. R. Haggenmueller, C. Guthy, J. R. Lukes, J. E. Fischer, K. I. Winey, *Macromolecules* 2007, **40**, 2417–2421.

29. H. J. Goldsmid, *Proc. Phys. Soc. B* 1956, **69**, 203.

30. H. Rathnayake, J. Binion, A. McKee, D. J. Scardino, N. I. Hammer, *Nanoscale* 2012, **4**, 4631–4640.

31. B. A. Jones, A. Facchetti, M. R. Wasielewski, T. J. Marks, *J. Am. Chem. Soc.* 2007, **129**, 15259–15278.

32. J. E. Anthony, *Chem. Rev.* 2006, **106**, 5028–5048.

33. B. Neises, W. Steglich, *Angew. Chem. Int. Ed. Engl.* 1978, **17**, 522–524.

34. Y. Che, A. Datar, K. Balakrishnan, L. Zang, *J. Am. Chem. Soc.* 2007, **129**, 7234–7235.

35. A. Datar, K. Balakrishnan, X. Yang, X. Zuo, J. Huang, R. Oitker, M. Yen, J. Zhao, D. M. Tiede, L. Zang, *J. Phys. Chem. B* 2006, **110**, 12327–12332.

36. M. Pope, C. E. Swenberg, *Electronic Processes in Organic Crystals and Polymers*; Oxford University Press, 1999, 39-48.

37. D. Chirvase, Z. Chiguvare, M. Knipper, J. Parisi, V. Dyakonov, J. C. Hummelen, *J. Appl. Phys.*, 2003, **93**, 3376-3383.

38. W. Bru¨tting, S. Berleb, A. G. Mu¨ckl, *Organ. Electron*., 2011, **2**, 1.

39. V. D. Mihailetchi, J. Wildeman, P.W. M. Blom, *PRL* 2005, **94** (126602), 1- 4.

40. P. S. Taylor, L. K-, Karasz, E. Wilusz, P. M. Lahti, F. E. Karasz, *Synthetic Metals*, 2013, **185-186**, 109-114.